Solar Energy 225 (2021) 784–801

Contents lists available at ScienceDirect

Solar Energy

journal homepage: www.elsevier.com/locate/solener

A non-intrusive optical approach to characterize heliostats in utility-scale power tower plants: Flight path generation/optimization of unmanned aerial systems

Tucker Farrell, Kidus Guye, Rebecca Mitchell, Guangdong Zhu *

National Renewable Energy Laboratory, 15013 Denver West Parkway, Golden, CO, USA

ARTICLE INFO

Keywords:
Concentrating solar power
Unmanned aerial system
Heliostat optical errors

ABSTRACT

A newly developed *in situ* non-intrusive optical (NIO) approach has been developed to survey various types of heliostat optical errors for a concentrating solar power (CSP) tower plant. To measure mirror surface slope error, facet canting error, and heliostat tracking error at a sub-milliradian accuracy, NIO requires several reflection images scanned over each individual heliostat. For a utility-scale plant that typically includes more than 10,000 heliostats, an unmanned aerial system (UAS) is crucial for efficient implementation of the NIO method. In this paper, we develop a flight path generation/optimization algorithm to plan more efficient UAS paths to collect NIO data over a utility-scale heliostat field. The algorithm considers NIO data requirements, all potential constraints, optimization within each subfield, and operational flexibility. Case studies are presented to illustrate the feasibility and robustness of the developed flight path algorithm. The path planning algorithm may also find applications elsewhere, such as drone-driven imaging under extreme conditions.

1. Introduction

Concentrating solar power (CSP) is a renewable energy technology that uses mirrors to reflect and concentrate solar energy so that it may be converted and stored as thermal energy. The thermal energy can then be directly used as process heat, be converted into electricity through thermodynamic cycles, or be used in generating solar fuels. In the case of power tower CSP, a field of heliostats, or mirrors that track the sun in two dimensions, focus sunlight at a tower receiver. For example, the 110-MW_e CSP plant at Crescent Dunes in Nevada, depicted in Fig. 1a, consists of a field of more than 10,000 heliostats spanning 1.2 km^2.

A heliostat, shown in Fig. 1b, is made up of discrete mirror facets in a grid pattern that can be canted or curved to a focal length that depends on its distance from the receiver. Errors in the heliostat shape and orientation causes optical degradation, which can have severe negative impacts on plant performance and costs. Optical errors include mirror non-specularity, mirror slope error, facet canting error, heliostat tracking error, and atmospheric attenuation (Kincaid, 2018). Simulations using the ray tracing software SolarPILOT have shown that the optical efficiency of a commercial heliostat field can decrease by as much as 20% when slope error (or slope error equivalent) increases by 2 mrad (Wagner and Wendelin, 2018).

The ability to measure and correct heliostat optical errors is essential to improving plant performance and allowing for the economic viability of CSP power tower technology. Yet, for a commercial-sized field containing thousands of heliostats, efficiently and accurately surveying the optical performance of every heliostat is a daunting task (Stynes and Ihas, 2012; Stynes and Ihas, 2012; Ren, 2014). Existing methods to characterize heliostat optical errors are not feasible for a full-field survey because they either require time-intensive manual calibration and operation, or do not provide enough information about the individual optical error sources (King, 1982; Strachan, 1992; Belhomme, 2009; Arqueros et al., 2003; Röger et al., 2008; Paré, 2002; Prahl, et al., 2011). For example, beam characterization systems (BCS) measure the flux density of the reflected beam by a heliostat (King, 1982; Strachan, 1992; Strachan and Houser, 1993); deflectometry uses imaging to assess the reflection of a striped pattern reflected by the collector (Ulmer, et al., 2011), and celestial-body-based reflective imaging uses the sun, moon, and stars as reference points to calculate tracking errors (Arqueros et al., 2003; Goldberg, 2015; Goldberg and Zisken, 2015). None of these methods are suitable for the large-scale survey that is required to assess the optical performance of a utility-scale plant.

The non-intrusive optical (NIO) method has been developed to provide this urgently needed large-scale *in situ* optical characterization (Mitchell and Zhu, 2020; Mitchell and Zhu, 2020). The NIO method uses

* Corresponding author.
E-mail address: Guangdong.Zhu@nrel.gov (G. Zhu).

https://doi.org/10.1016/j.solener.2021.07.070
Received 13 April 2021; Received in revised form 13 July 2021; Accepted 30 July 2021
Available online 6 August 2021

Nomenclature

ϕ_{az}	Heliostat azimuth
ϕ_{el}	Heliostat elevation
x_h	Heliostat position
$\hat{x}_{hn}$	Heliostat surface normal vector
h_w	Heliostat width
h_l	Heliostat length
$\vec{x}_h^t$	Vector from heliostat to tower
$\vec{x}_s^t$	Vector from sun to heliostat
θ	Angle of reflection
x_t	Tower position
b_u	Upper bound for lens effective range
h_{fov}	Heliostat field-of-view angle
d_{vert}	Required vertical distance along a vector
d_{space}	Vertical spacing between a heliostat's bottom edge and an obstructing heliostat's top edge
$G(n)$	Immediate cost of selecting node n
n	A node in a graph when computing paths
$f(n)$	Total cost of choosing node n in the NIO context
$t_n(n)$	Time required to transit to node n + 1 from node n
x_{base}	Base station location
t_{UAS}	Flight endurance of the UAS in seconds
h_{FOV}	Camera field-of-view angle
f	Camera lens focal length
d_l^{ub}	Camera lens effective distance upper bound
d_l^{lb}	Camera lens effective distance lower bound
c_d	Camera distance to point of interest
t	Time
t_{open}	Time at which heliostat becomes measurable
t_{close}	Time at which heliostat is no longer measurable
$\hat{x}$	Unit vector
d_{sensor}	Camera sensor size in mm
b_l	Lower bound for lens effective range
x_{UAS}	UAS position
$\hat{k}$	K-component of vector in i, j, k notation
$F(n)$	Total cost of selecting node n
$H(n)$	Heuristic cost of selecting node n
x_{node}	Node position
$t_b(n)$	Time required to return to base station from node n
$h_n(n)$	Time heuristic related to the remaining time before node n is no longer measurable
v_{uas}	UAS velocity
$t_{elapsed}$	Elapsed time since UAS take-off in seconds

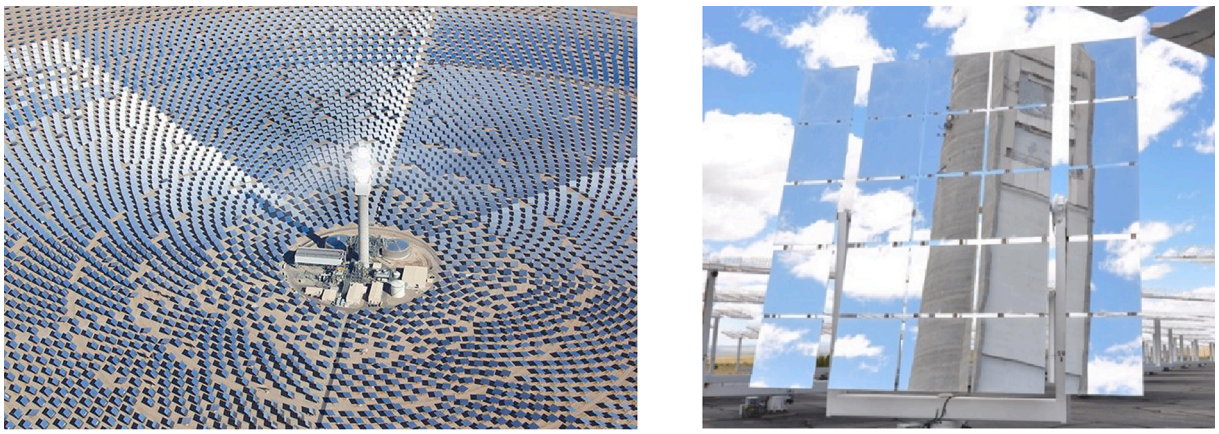

(a) (b)

Fig. 1. (a) Photo of a SolarReserve heliostat field at Crescent Dunes, Nevada (Olewitz, 2016); (b) Example image of a heliostat taken at National Solar Thermal Test Facility (NSTTF) (Mitchell and Zhu, 2020).

an unmanned aerial system (UAS) to efficiently collect image data of the heliostats with the reflection of the tower structure, as illustrated by Fig. 2. These images are post-processed using photogrammetry and image processing techniques to calculate slope, tracking, and canting errors.

Autonomous UAS path planning is an integral part of the NIO method because the camera must be positioned at precise waypoints to capture viable reflection images of thousands of heliostats while considering that certain heliostats are more suited for measurement at certain times of day due to their relative orientation to the tower. Drone waypoints must be chosen to photograph all heliostats within measurability constraints while minimizing total travel time. Existing autonomous path planning algorithms optimize the path, given a series of targets. For example, path planning can be reformulated as a "traveling salesman" problem and solved computationally with static (Obermeyer, 2009) or dynamic conditions (Ferris, 2018). The A* Algorithm is a widely used path optimizer that defines targets as nodes in a weighted graph and exhaustively searches for a path that minimizes a cost function. Modifications of A* can improve its speed, such as dynamically replanning the path based on new search information (Likhachev, 2005), sorting target nodes into regions (Ishida et al., 2019), and prioritizing multiple goals (Davidov and Markovitch, 2006).

In this paper, an algorithm is presented to calculate a drone path to perform an image survey of a utility-scale heliostat field that satisfies the measurability constraints of the NIO method. Throughout, algorithm results from the National Solar Thermal Test Facility (NSTTF) are presented as demonstration and validation. Section 2 gives an overview of the NIO method. Section 3 outlines the complete drone pathing algorithm. Subsections 3.1–3.3 describe the input parameters required to build a field model, and the measurability constraints that must be satisfied by the drone path. Subsection 3.4 details how the field is divided into subregions, and Subsection 3.5 describes how a path of target heliostats is determined using A*. Subsections 3.6 and 3.7 explain how waypoint positions are calculated for individual heliostat targets and outputted. Section 4 gives results of the algorithm for the Crescent Dunes utility-scale plant. Section 5 provides discussion of the strengths

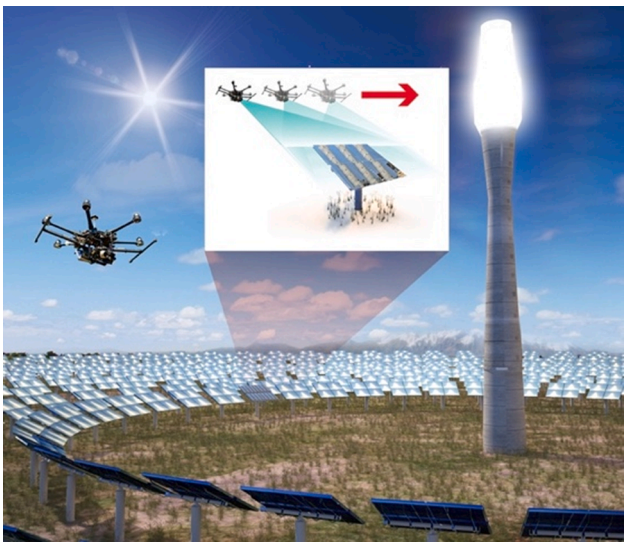

Fig. 2. Illustration of the UAS image data collection for the NIO method (Mitchell and Zhu, 2020).

of the method along with ongoing work to improve the method. Section 6 summarizes the main conclusions of the analysis.

2. NIO method

The NIO method is a proposed approach to characterizing heliostat errors in CSP tower plants. These errors can be categorized into canting errors and slope errors that affect individual facets, and tracking errors that affect the entire heliostat, illustrated by Fig. 3a. The NIO method uses UAS collected images of the reflected tower in the heliostat surface, like the example image shown in Fig. 1b, to detect distortions in the mirror surface. Given a known camera, tower, and heliostat position, the detected position of the reflected tower edge in the images can be compared with the known ideal reflected edge position to calculate the optical errors, illustrated by Fig. 3b.

For a detailed explanation and validation of the NIO method, refer to (Mitchell and Zhu, 2020). For a sensitivity analysis of the method, see (Mitchell and Zhu, 2020). The primary steps of the NIO method include:

1. Perform data collection with a UAS to obtain images of the reflected tower edge traversing the heliostat surface.
2. Use image processing techniques to detect the positions of the heliostat, the individual mirror facets, and the reflected tower edge in each image.
3. Use photogrammetry techniques to calculate the position and orientation of the camera relative to the heliostat.
4. Use knowledge of the heliostat azimuth and elevation position and the tower position and geometry to calculate the position of the tower edge relative to the heliostat.
5. Calculate slope, canting, and tracking errors.
6. Perform refinements to the assumed tower position and optical error calculations based on results.

For the NIO method to be successful, the collected images must show an unobstructed view of the tower edge spanning the full heliostat aperture, like the image shown in Fig. 3b and Fig. 1b. The images also must show both edges of the tower traverse the full surface of each mirror facet, so that reflection data is provided for the full heliostat surface. The subsequent sections explain how the drone pathing algorithm accomplishes Step 1 of the NIO method with these imaging constraints for all heliostats in a commercial-sized CSP plant.

3. UAS flight path algorithm

The UAS flight path is computed using information describing the CSP installation, the time of the measurements, and the UAS performance metrics. Fig. 4 shows the framework for planning a series of flights through CSP installation as well as all required input data and the output format. Each step performs operations on individual heliostats that impacts the UAS path over the entire field. The current section provides data regarding the application of the method and example output for single heliostats. The subsequent results and discussion section will present a macro view of algorithm's application to the NSTTF as an example implementation.

3.1. Input parameters

The input parameters for collecting NIO image data describe the field layout, tower properties, UAS properties, and time data.

Accurate heliostat physical properties are necessary to properly position the camera aboard the UAS. Along with the location, the parameters listed below allow the algorithm to accurately calculate distances and angles at which the camera can capture a usable image. NIO input parameters for heliostats, tower, field layout, the UAS, and camera are displayed in Table 1.

The facet layout, height, width, and gap size are used to accurately

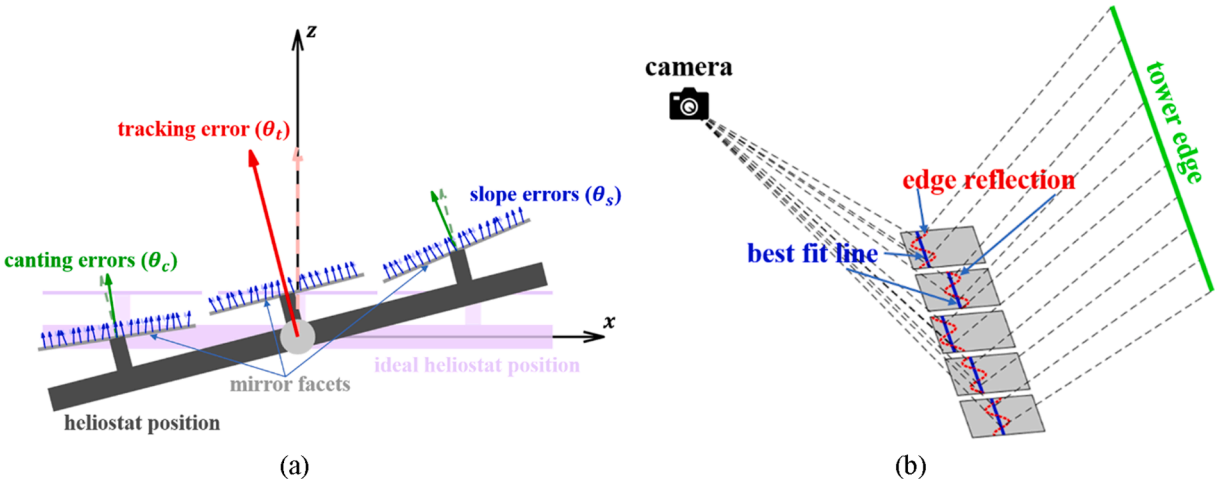

Fig. 3. (a) Illustration of optical error types measured by the NIO method: slope errors, canting errors, and tracking errors. (b) Illustration of the way the NIO method uses the known camera, heliostat, tower, and reflected tower edge positions to calculate optical errors in the mirror surface.

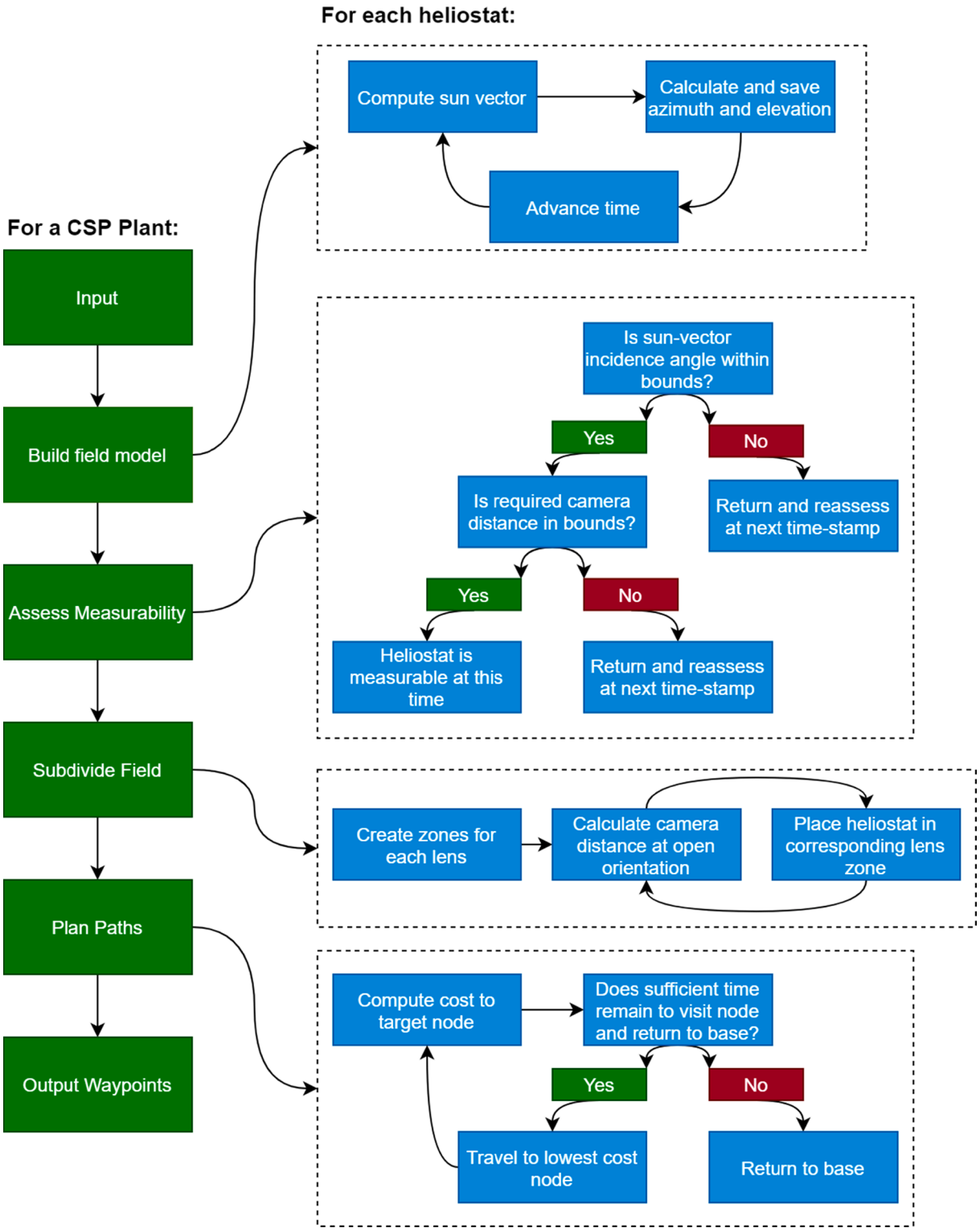

Fig. 4. UAS flight planning diagram.

size the heliostat surface, while the pedestal height and rotation axis offset allow the algorithm to locate the middle of the surface in space.

The tower parameters impact the calculation of the heliostats' expected orientations, as well as positions to map reflection data to in space. The tower parameters below are input to allow accurate computation of the heliostat orientations given a specific time.

The tower physical dimensions allow computation of heliostat orientations while the location in space allows the algorithm to calculate waypoints in a local coordinate frame, right-handed East (+X), North (+Y), Up (+Z), and transform into a global coordinate frame before upload to the flight computer.

3.2. *Build a field model*

The field model consists of a map built from the tower and heliostat position data that encompasses the dynamic input parameters listed in

Table 1
NIO path-planning input parameters.

Heliostat Parameters	Tower Parameters	Field Layout	UAS	Camera
Facet layout Facet height and width Facet gap size Pedestal height Rotation axis offset	Tower height to the receiver Receiver height Tower diameter Tower geometry Tower geodetic coordinates Elevation at the base	Local X, Y, Z of heliostats relative to the tower base	Cruise velocity Endurance	Sensor size Resolution Focal length

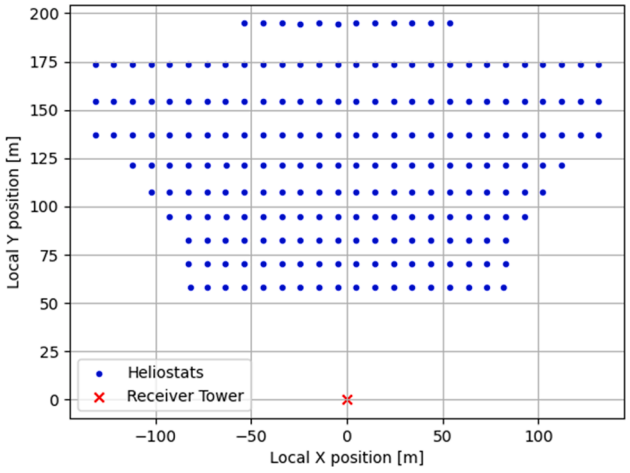

Fig. 5. Layout of NSTTF CSP heliostats and receiver tower.

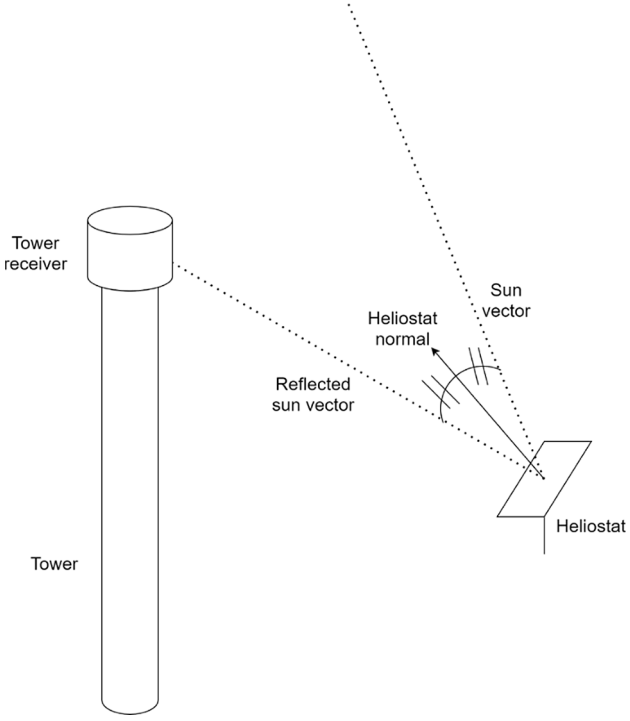

Fig. 6. Heliostat normal is the angle bisector of the sun vector and reflected sun vector.

Table 1. An output map of the NSTTF facility is shown in Fig. 5.

Computing the expected orientation of the heliostat given a date and time is the first step in collecting NIO image data, as noted in Fig. 4. The orientation of the heliostat is used to accurately position the UAS such that the tower edges are visible in the reflection.

The method for finding the expected heliostat orientation can be seen in Fig. 6. The heliostat orientation is dynamic and therefore must be recomputed at a specified time interval. This interval gives the effective resolution of the field map.

The algorithm assumes the heliostat is oriented to reflect the sun vector from the center of the heliostat to the center of the receiver as default but may change as needed. The required orientation for this to occur is such that the unit vector of the heliostat normal, $\hat{x}_{hn}$, is the angular bisector of the sun vector $\vec{x}_s^t$ and the vector drawn from the heliostat center to the receiver center, $\vec{x}_h^t$.

$$\vec{x}_h^t = x_t - x_h \tag{1}$$

Then, by adding the normalized vectors, the normalized resultant is the heliostat's normal unit vector:

$$\hat{x}_{hn} = \frac{\hat{x}_h^t + \hat{x}_s^t}{\left|\left|\hat{x}_h^t + \hat{x}_s^t\right|\right|} \tag{2}$$

The heliostat normal in cartesian coordinates can be translated into an azimuth angle, ϕ_{az}, and elevation angle, ϕ_{el}, using the components of the heliostat unit vector. In the field local coordinate system, azimuth is represented as positive north of east.

$$\phi_{az} = \tan^{-1}\left(\frac{\hat{x}_{hn}^y}{\hat{x}_{hn}^x}\right) \tag{3}$$

$$\phi_{el} = \sin^{-1}\hat{x}_{hn}^z \tag{4}$$

In a CSP tower plant, the heliostat orientation is time-variant under operation. The orientation changes to focus solar energy on the receiver as the sun vector direction evolves throughout a specified day. The orientation of the heliostat described by its azimuth and elevation is illustrated in Fig. 7. The azimuth is given in degrees clockwise from true North, and elevation in degrees above the horizon. The sun position is calculated based on the Crescent Dunes tower base at 38.239 degrees latitude, −117.364 degrees longitude, and 1497.17 m above mean sea level.

3.3. Apply measurability

Several operational constraints must be met during image collection to ensure the images are appropriate for NIO post-processing. The constraints on measurability are due to:

- Camera incidence angle on the target heliostat
- Blocking from neighboring heliostats
- Camera resolution and lens
- UAS altitude to avoid collision
- Wind speed and direction
- Solar flux from reflected thermal energy.

3.3.1. Camera angle

A bound must be placed on the angle between the heliostat normal and the incident camera vector. As heliostats reflect the sun vector to the tower, the camera is very nearly aligned with the sun vector, and so the sun vector incidence angle may be used to indicate if the heliostat is in a measurable orientation. The bound prevents the image of the heliostat becoming so oblique that it is unusable in the post-processing software. In this paper, the bound is set to 60 degrees, though the limits of the

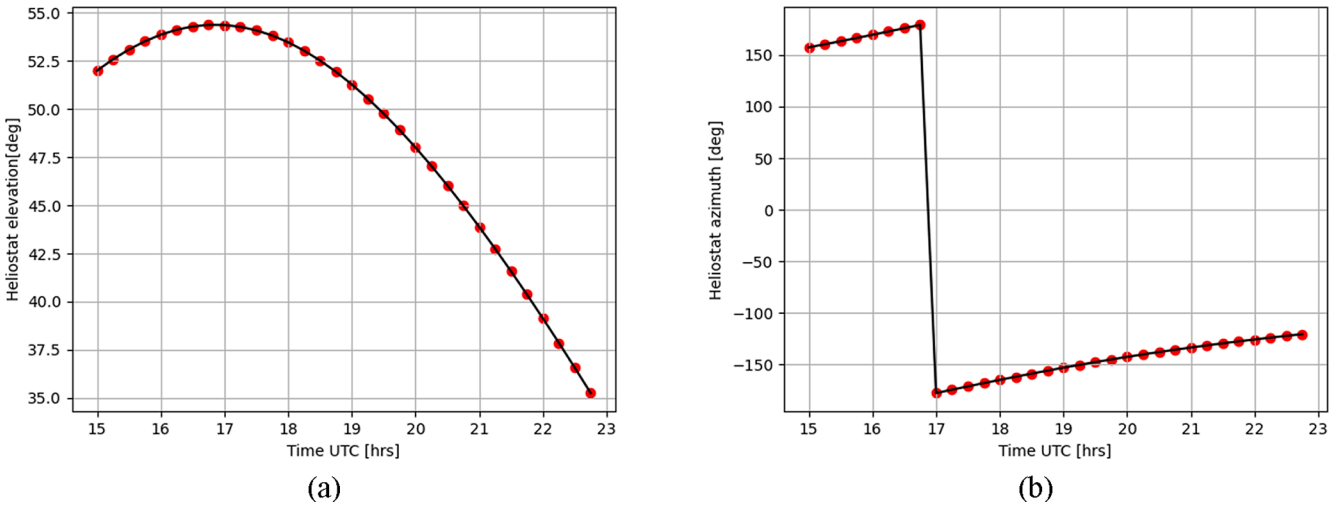

Fig. 7. Sun-tracking elevation (a) and azimuth (b) for a single heliostat: 15-minute intervals, June 21, 2020 14:00–22:00 UTC (PDT + 7).

computer vision post-processing are being more closely researched.

3.3.2. Camera resolution and lens

The camera resolution and lens are linked to the distance from which the UAS may acquire a usable image. For an individual field, the effective range for a lens can be computed using the heliostat size, lens focal length, and camera sensor size.

For consistency, all calculations are done in 35-mm equivalent focal lengths. For crop sensors, the published focal length must be multiplied by the sensor's crop factor before performing calculations.

User-defined bounds are placed on the size of the heliostat in the image. In this example, we limit the ratio of the heliostat's longest dimension to the camera sensor's shortest dimension to between 50% and 90%. These bounds can be transformed into a usable range for a specified focal length. The bounds are expressed as a user-defined ratio of the camera's FOV, b_l and b_u and are used to manipulate the pixel resolution of the heliostat in the frame and ensure neighboring heliostats are not introducing glare from the reflected receiver.

The ratios conservatively compare the heliostat's largest dimension with the camera's shortest FOV. The upper and lower range of a lens, d_l^{ub}, d_l^{lb}, given its focal length f and sensor size d_{sensor} in millimeters are then:

$$FOV = 2\tan^{-1}\left(\frac{\min(d_{sensor})}{2f}\right) \tag{5}$$

$$d_l^{ub} = \frac{h_w}{2b_u\tan\left(\frac{FOV}{2}\right)} \tag{6}$$

$$d_l^{lb} = \frac{h_w}{2b_l\tan\left(\frac{FOV}{2}\right)} \tag{7}$$

In, we use the noted focal lengths and associated effective imaging ranges for a Crescent Dunes heliostat with dimensions of 10.42 × 11.65 m and an NSTTF heliostat with dimensions of 6.3502 × 6.8074 m

The camera used is a 24.4-MP camera with an APS-C sized sensor measuring 23.5x16.6 mm.

3.3.3. Blocking

Blocking occurs when the reflected image in a heliostat is fully or partially obstructed by neighboring heliostats. Blocking is affected by heliostat orientation and camera positioning. To determine if a heliostat is in an unblocked orientation, the following constraints must be satisfied:

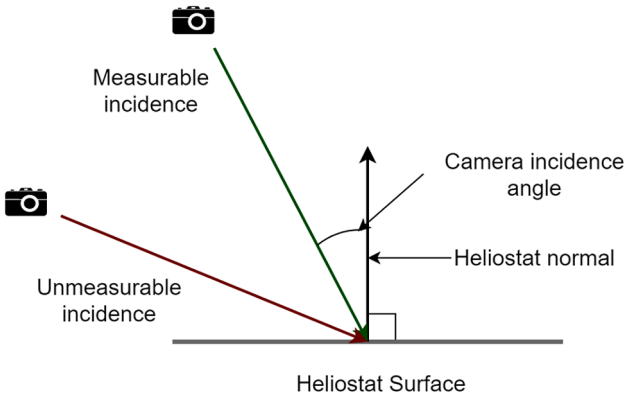

Fig. 8. Camera incidence angle.

Table 2
Sample lens and effective ranges.

Focal Length (35 mm equivalent)	Effective Imaging Range (meters) Crescent Dunes Heliostat	Effective Imaging Range (meters) NSTTF Heliostat
30	15.9 to 28.6	9.5 to 17.1
45	23.8 to 42.9	14.2 to 25.6
75	39.7 to 71.5	23.7 to 42.7
127.5	67.6 to 121.6	40.3 to 72.5

- The camera distance must be at or below the maximum effective distance of the longest lens.
- The top reflected vector must reach the tower below the receiver (see Fig. 8).
- The bottom reflected vector must have an adequate elevation to clear neighboring heliostats (see Fig. 8).

To assess blocking, the camera distance is fixed at the maximum allowable and clearance is assessed by considering potential obstructing neighboring heliostats. For each heliostat, the potential obstructing neighbors are identified. The target heliostat is checked for neighbors that interfere with the heliostat's FOV of the tower, using the FOV of the camera at its maximum effective range, as seen in Table 2. The effective range is controlled by defining the maximum and minimum occupation of the camera FOV, as seen in Fig. 9. Given the camera range to the heliostat, the FOV of the heliostat to the tower, h_{FOV} , can be computed

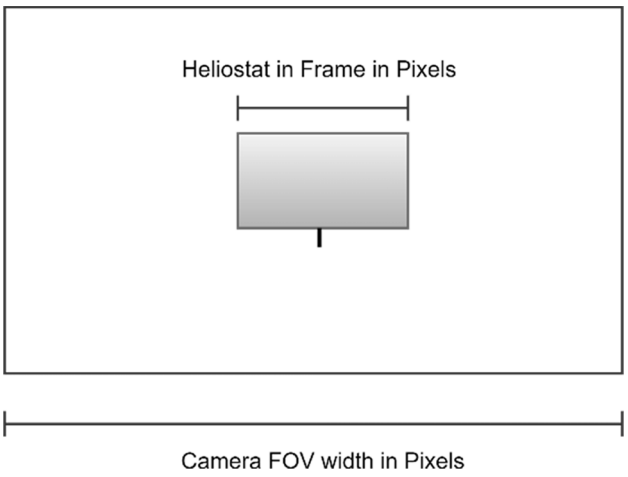

Fig. 9. Heliostat size and resulting resolution in given camera field of view (FOV).

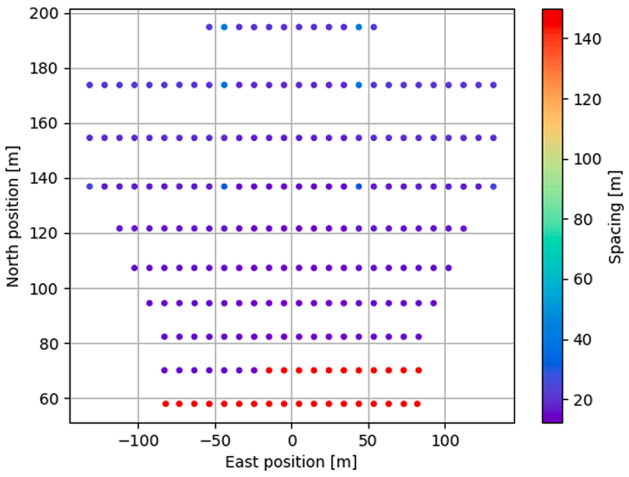

Fig. 11. Effective spacing between target heliostat and neighboring heliostats obstructing the view of the tower.

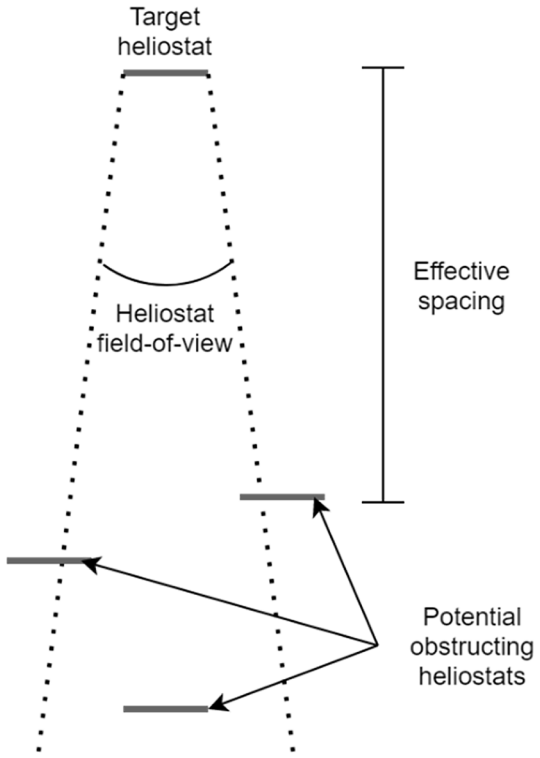

Fig. 10. Identifying potential obstructions to the target heliostat's FOV.

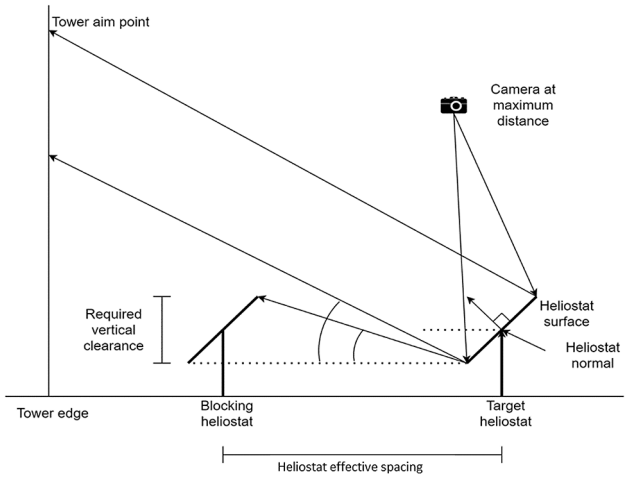

Fig. 12. Heliostat with adequate clearance to acquire a clear view of the tower edge.

by:

$$h_{FOV} = 2\tan^{-1}\left(\frac{h_w}{2c_d}\right) \tag{8}$$

If a neighboring heliostat may interfere with the view of the tower, as in Fig. 10, it is saved as an obstruction.

Given a set of potential obstructions, the spacing to these obstructions is computed. For each heliostat, the effective spacing to measure that heliostat is computed and seen in Fig. 11. The nearest potential obstruction is used to calculate whether the target heliostat is measurable at a given time and orientation. Each heliostat's effective spacing and orientation determine if a clear view of the tower can be achieved. If a clear view can be achieved at the maximum allowable camera distance, the heliostat is not blocked at that orientation. Fig. 12 below

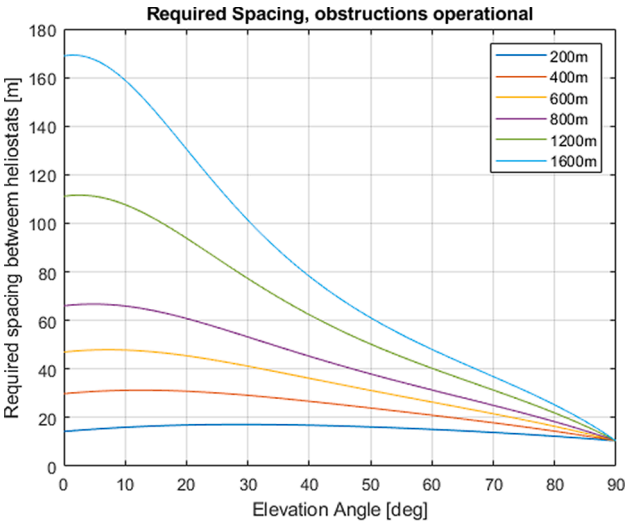

Fig. 13. Effect of heliostat elevation on required spacing to clear obstructions.

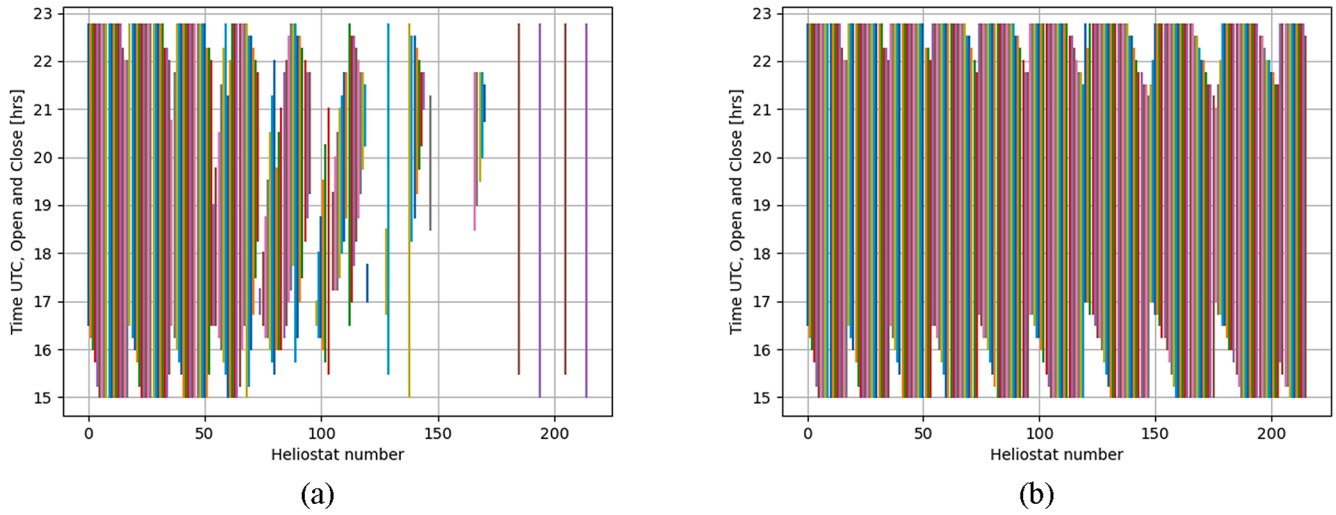

Fig. 14. Measurability windows for NSTTF's 210 heliostats, both operational (a) and stowed (b).

shows a heliostat in an unblocked position, where the reflected angle off the bottom edge of the heliostat, θ_{rb}, is greater than θ_{rmin}, the minimum required elevation of the vector reflected from the heliostat's bottom edge for clearance.

The heliostat elevation angle is closely related to the heliostat's range, or distance away from the tower. At low elevation angles, the heliostat may be prohibitively difficult to measure while the neighboring heliostats are in operation, as seen in Fig. 13.

In several cases, a measurable orientation may not be achievable in an operational plant for a given day. The target heliostat may not enter an orientation that gives a clear view of the target point on the tower, or the required camera distance to achieve the desired image is infeasible. In this instance, the blocking heliostats must be stowed, or some blocking of the target heliostat must be accepted, which will result in a partial measurement. The target heliostats are then given measurement windows ignoring obstructions and flagged during the path-planning process.

Imposing the above constraints on the NSTTF plant for an 8-hour period on June 21, 2020, at a 15-minute resolution yields the measurement windows seen in Fig. 14. The shown measurement windows are vertical lines for each heliostat in the field, alternating colors for clarity. A heliostat "open" time is defined when at time t, the heliostat is measurable, and at time t-1, the heliostat is not measurable. A heliostat "close" time is the reverse, when at time t the heliostat is not measurable, but at time t-1, it is measurable. In all cases, the lower point on the vertical line is the "open" time and the upper point the "close" time. Measurement windows are computed assuming the plant is operational, which bounds the heliostat's orientation to the position of the sun, and assuming the heliostats may be manipulated or stowed.

3.3.4. UAS altitude

UAS altitude must be restricted to between the upper bounds of legislative bodies and a lower bound, ensuring the UAS will not impact any heliostats during operation. These parameters will vary between installations and are set by the operator. At the time of this writing, the FAA limits UAS operations to an altitude of 400 feet above ground level.

3.3.5. Wind speed and solar flux

Wind speed and direction must be considered if operating outside of the UAS's published operational constraints. Should experimental data show excessive drift in the UAS position or tracking, more consideration will be given to the wind. At this time, modern UAS commonly operate in wind speeds up to 30 mph, which is above and beyond the safe operational limits for Crescent Dunes solar power plant. At these speeds, the heliostats are stowed flat and are not measurable. Wind poses a more significant concern for customized flight controllers and autopilots.

The solar environment above a CSP field as it relates to the UAS is an ongoing topic of research.

Table 3
User-defined parameters and effects.

Parameter	Description	Effect
Camera incidence angle	User may define higher or lower acceptable incidence angles for image collection.	Lower incidence angles will result in less oblique images but will constrain measurability.
Camera lens bounds	User may define the acceptable size of the heliostat in the collected image.	A tighter bound creates a tighter allowable range for the lens. A small lower bound allows the camera to be further away from the heliostat, while a high upper bound allows the camera to be closer.
Scanning time	The user may impose a scanning time limit on the UAS.	A lower scanning time will lower the number of images received per heliostat, as a function of the camera's shutter speed or frame rate.
Reflection coverage	The user may accept some blocking conditions and opt for partial reflection coverage (top or bottom half).	Blocking conditions will not deem a heliostat unmeasurable. To receive measurements of the bottom half, the aimpoint is traced to the heliostat center. The heliostat should not be operational in this case, as the receiver will be visible in the reflection and blind the camera.
Lens selection	The user may opt to use a single focal length lens or combination of lenses.	Longer lenses offer more coverage, shorter lenses are more readily available. Very few commercially available UAS feature interchangeable lenses. Lens focal length is linked closely to blocking conditions.

3.3.6. Optional constraints

The path-plan may be customized further with operator-defined parameters. A list of tunable parameters and the resulting effect on blocking, the path, and image collection can be seen in Table 3.

3.3.7. Offline operation

Conditions may exist that require the UAS to scan offline heliostats. Maintenance periods, calibrations, or manipulation of heliostats in

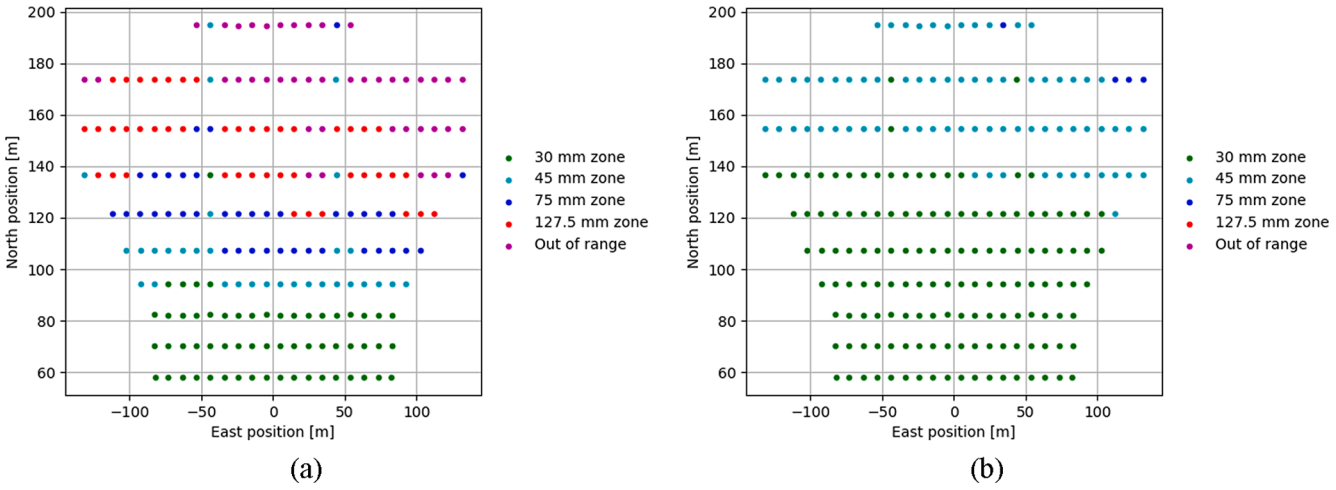

Fig. 15. Heliostats placed into focal length-associated measurement zones at NSTTF while operational (a) and stowed (b).

positions difficult to measure require that the algorithm adjust to receive adequate data. In the case of blocked heliostats, obstructions may be briefly stowed to allow a wider FOV. Offline heliostats may be reoriented into desirable positions within a defined measurable range to achieve measurements. Operators may adjust the algorithm to include or exclude these heliostats in the path and calculate waypoints based on designed orientations or stowed obstructions.

3.4. Subdivide field

Commercial installations may employ over 10,000 heliostats over a vast land area. The maximum flight time for a single UAS is commonly 20–40 min due to the limited battery capacity. A single continuous path through the entire field is not a practical proposition. The field is first divided into attainable subfields. The drone path over each subfield may be computed for the same day, allowing several UAS to operate concurrently, or may be computed for sequential days, completing the testing more slowly, but with fewer UAS-associated equipment and operation costs. Dividing the field also allows operators to correct for variations, handle delays, or manage weather conditions without requiring operators to recompute the entire flight path.

Section 3.3.2 outlines the determination of the focal length effective range. This effective range for each lens is the governing parameter for placing heliostats in focal zones. The heliostat camera distance is computed at the heliostat's orientation with the highest elevation. This distance is used to place the target heliostat into the zone corresponding with the appropriate lens. This camera distance, d_c^z, is the camera distance used to place the heliostat in a measurement zone and is calculated in the same manner as the central waypoint in Section 3.6.1. See Fig. 18 and Eq. (14) through Eq. (19) for computing x_{UAS} and the distance $||x_t||$.

If d_c^z is within the bounds set for any of the selected lenses, the heliostat is placed into that zone. See Fig. 15 for heliostats at NSTTF placed into measurement zones.

3.5. Plan paths

Using the orientation and blocking data, a schedule can be generated to measure each of the selected heliostats. The order of the heliostats is subject to each heliostat's measurability and overall flight mission priority and efficiency. The measurability is represented as a function of the heliostat's orientation, time of day, and resulting blocking criteria. The path is planned through the heliostats using a modified version of the A* heuristic search algorithm discussed in the following section.

The fundamental A* algorithm operates according to Eq. (8) through Eq. (12) below. The total cost F of progressing to node n is represented by an immediate cost, G, and a heuristic estimate of that node's effect on the remaining path, H. In its original formulation presented by Hart, Nilsson, and Raphael, the costs and heuristics are represented by distances to find the shortest path through a directed graph (Peter Hart and Raphael, 1968). The cost of traveling to node n is the distance to that node $G(n)$, plus the estimated remaining path, $H(n)$, from node n to the goal.

$$F(n) = G(n) + H(n) \tag{9}$$

When applied to NIO, the time variance of the field, endurance of the UAS, and the length of the day make attention to time more pertinent than attention to distance traveled. For the NIO context, each heliostat is a node. The NIO path-planner then takes in the relevant parameters listed above and aims to find a path through a given set of nodes. As in the A* framework above, the planner is striving to find a balance between immediate, greedy rewards by minimizing the flight time between immediate nodes, and a long-term, heuristic reward by visiting heliostats before they close, and avoiding a long transit back to the base.

In this instance, we modify the previous equation to consider a time-related cost:

$$f(n) = t_n(n) + t_b(n) + h(n) \tag{10}$$

Here, t_n is the time required to transit to node n at the UAS's speed parameter, dependent on the position of the node x_{node} and UAS velocity v_{UAS}, t_b is the time to return to the base station, dependent on the base station position x_{base}, the UAS flight endurance, t_{UAS}, and the elapsed flight time, $t_{elapsed}$, and h is the time cost imposed by the heliostat's measurability window, seen in Equations (10) through (12), where t is the current time of day, t_{open} is the time at which the heliostat becomes measurable, and $t_{close}$is the time at which the heliostat is no longer measurable. All time is measured in seconds from time 0, which signifies the beginning of a scan day.

$$t_n(n) = \frac{x_{node}}{v_{UAS}} \tag{11}$$

$$t_b(n) = \frac{x_{base}}{v_{UAS}} - \left(t_{UAS} - t_{elapsed}\right) \tag{12}$$

$$h(n) = \begin{cases} t < t_{open} h(n) = \infty \\ t_{open} < t < t_{close} h(n) = t_{close} - t \\ t_{close} < t h(n) = \infty \end{cases} \tag{13}$$

This method produces costs for selecting subsequent nodes that limit the selection to measurable heliostats and prioritizes those heliostats close to the current position. The return-to-base cost t_b ensures the UAS avoids making decisions that will fly it prohibitively far from the desired

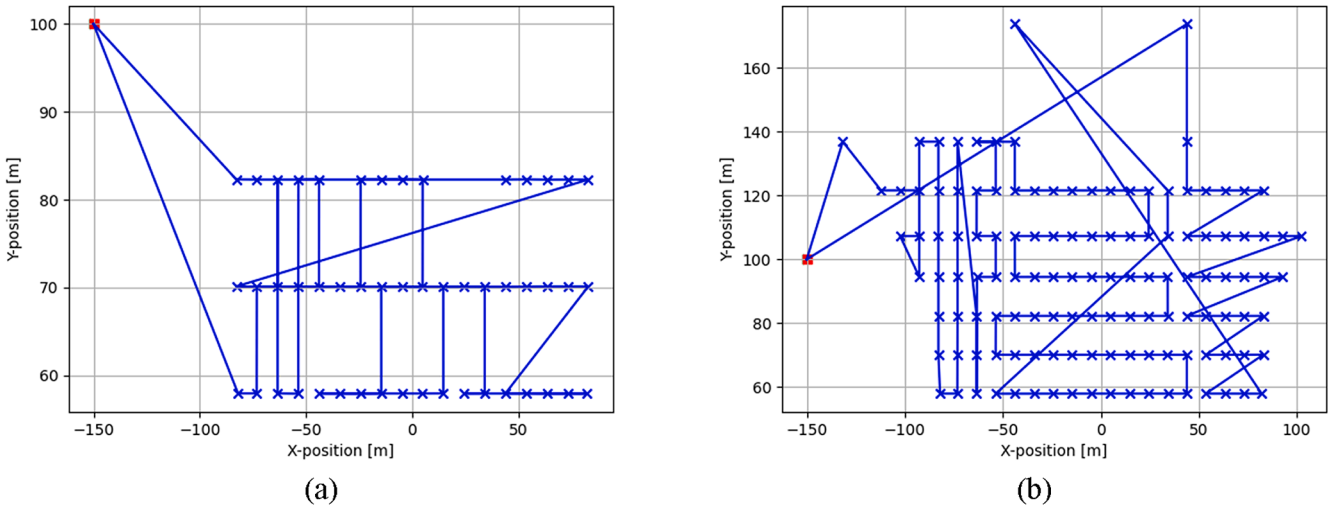

Fig. 16. NSTTF flight paths for heliostats placed in the near zone for an operational field (a) and obstructions stowed (b).

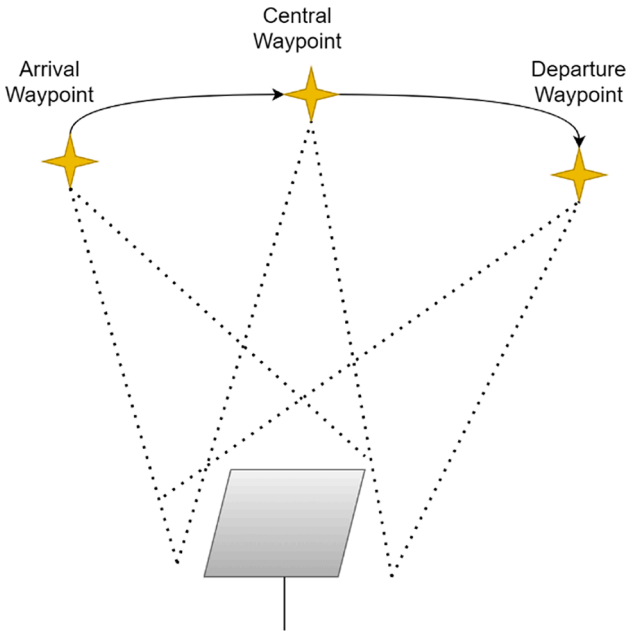

Fig. 17. Single heliostat waypoint sequence.

landing position, wasting time in transit. The result is a cost that effectively drives the UAS to prioritize time spent measuring over time spent transiting, while limiting its focus to those heliostats in measurable orientations.

Seen in Fig. 16 is a sample flight plan for a single day over the NSTTF near-zone heliostats. In this figure, the sun vector is incident on the field in the negative X direction, or from the east. The planner prioritizes those heliostats in the west field and moves eastward. This effect is more pronounced in the utility-scale results in Section 4. The lower elevation angles and consequently shorter measurement windows in the west field result in a lower associated cost for targeting those heliostats. The base station in this scenario is stationary, placed 150 m west, 100 m north of the tower base, shown by the red dot in Fig. 16. The time constraint of the heliostat's measurement window has a variable impact on the path planner's decision making, resulting in some longer transits and irregular flight patterns.

3.6. Output waypoints

The output of the path generation function in Sections 3.4–3.5 is a subset of heliostats, scheduled according to the path planner algorithm. Each heliostat stores its measurement orientation, which is used to compute waypoints for the UAS. The UAS waypoint stores the required information for the UAS to accurately position itself and aim the camera and capture the NIO image data.

Each heliostat target is assigned three waypoints describing the path for the UAS to effectively scan the heliostat. The waypoints are defined as the arrival waypoint, central waypoint, and departure waypoint. The arrival waypoint is the point the UAS targets to arrive and begin the scan path. The central waypoint is used to position the UAS midway through the scan and map the reflection from the tower. The departure waypoint is the final waypoint at which the tower reflection finishes traversing the heliostat surface and is no longer visible. This is outlined in Fig. 17.

The result is the reflection of the receiver tower traversing across the surface of the heliostat, providing a complete, high-resolution dataset for image post-processing.

3.6.1. Compute central waypoint

Fig. 18 below outlines the calculation of the central waypoint. The waypoint is computed by mapping a designated aimpoint on the receiver tower (A) to the center of the heliostat's top edge (B). The waypoint then lies on the reflected vector from point (B) at such a distance that the vector reflected from point (C), is at the required elevation given by the heliostat's effective spacing computed in Section 3.3.3.

Clearance of obstructions is dependent only on the elevation of the reflected vector. Therefore, the required position of the UAS a specific distance along the top reflection vector $\overrightarrow{x_{top}}$ that results in adequate elevation in the bottom reflection vector $\overrightarrow{x_{bot}}$:

$$x_{UAS} = ||\overrightarrow{x_{UAS}}|| \widehat{x_{top}} \tag{14}$$

Where $||x_{UAS}||$ is the required distance in the direction $\widehat{x_{top}}$ to allow the vector reflected from the bottom edge of the heliostat to clear obstructions. The magnitude $||x_{UAS}||$ can be found by:

$$||x_{UAS}|| = \frac{d_{vert}}{\widehat{k_{top}}} \tag{15}$$

Where d_{vert} is the required vertical distance along vector x_{UAS}, and can be found using the z-direction, or k-components of the reflected vectors $\overrightarrow{x_{top}}$ and $\overrightarrow{x_{bot}}$, the vectors reflected off the top and bottom edges of the heliostat, and the required vertical spacing, d_{space}, defined as the vertical distance between the target bottom edge and the obstructing top

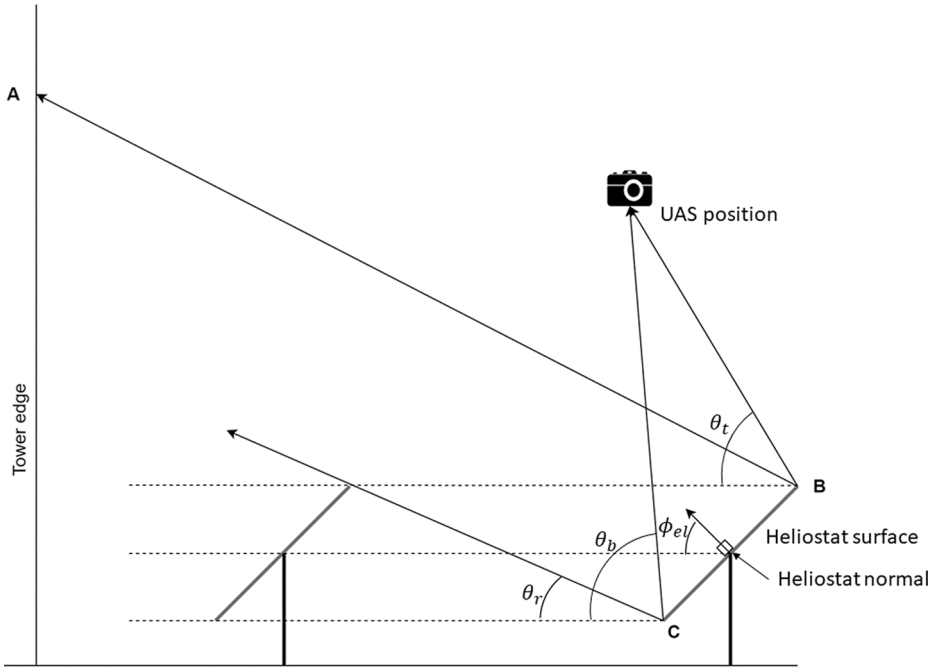

Fig. 18. Center waypoint elevation constraint on camera distance.

edge.

$$d\_vert = \frac{\widehat{k_{bot}}\left(d_{space}\right)}{\widehat{k_{top}} - \widehat{k_{bot}}} \tag{16}$$

The z-direction, or k-components of the unit vectors $x_{top}$and $x_{bot,}$are calculated by:

$$\widehat{k_{bot}} = \sin(\theta_{bot}) \tag{17}$$

$$\widehat{k_{top}} = \sin\left(\theta_{top}\right) \tag{18}$$

$$\theta_{bot} = 2\phi_{el} - \theta_{req} \tag{19}$$

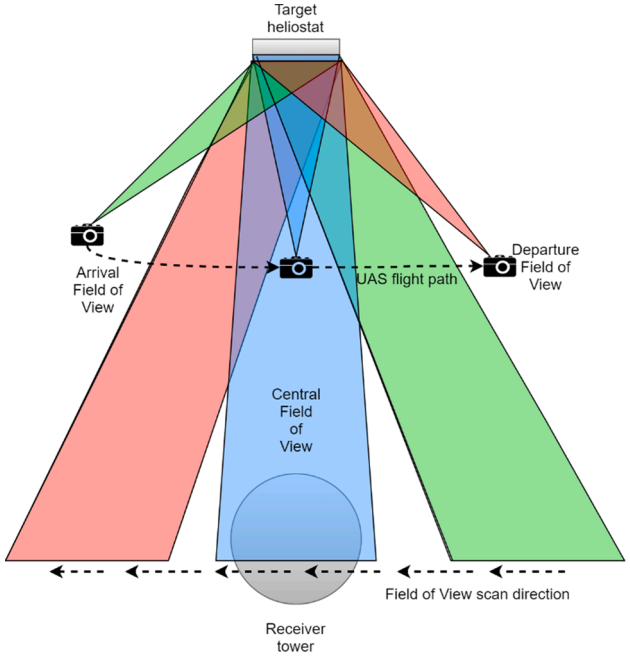

Fig. 19. Camera FOV scanning from arrival to departure (top-down view).

Where $\theta_b$and $\theta_t$are the angles noted in Fig. 18, $\theta_r$is the required clearance elevation, and ϕ_{el} describes the heliostat elevation angle.

3.6.2. *Compute arrival and departure waypoints*

The arrival and departure, or peripheral waypoints, allow the UAS to capture sequential images as the tower reflection traverses the surface of the heliostat. As the UAS traverses between the waypoints, the reflection of the tower is sequentially visible in each of the heliostat facets. This scanning behavior ensures that each facet has the visible tower data required for image processing. Fig. 19 shows the scanning in a plan view, showing the UAS FOV as it reflects off the target heliostat.

The peripheral waypoints are computed based on the initial center waypoint. The waypoints are designed to position the UAS such that the top aim point on the tower traverses across the top edge of the heliostat while the vertical reflected edge traverses across the heliostat surface. This allows for the widest FOV without incurring blocking by ensuring the longest length tower possible is visible. This minimizes the required UAS distance from the target. The angle of the tower image on the heliostat surface may vary based on the orientation of the heliostat, shown in Fig. 20. The variance in the angle governs the magnitude of the scan, where a vertical reflection requires a much shorter scan than obscured reflections.

The peripheral waypoints, given a central waypoint and target heliostat are calculated by finding the required change in reflection angle, $\delta\theta_{fov}$ below, to ensure the reflected tower image begins and ends the scan out of view. First, by assuming a vertical reflection and given the heliostat range to the tower, d_t, and the camera distance d_c, the required scan coverage d_{scan}^{min}can be found:

$$fov_{eff} = 2{\cdot}\tan^{-1}\left(\frac{h_w}{d_c}\right) \tag{20}$$

Which gives the length in meters encompassed by the FOV at the tower:

$$d_{fov}^{t} = 2{\cdot}\tan\left(\frac{fov_{eff}}{2}\right)(d_c + d_t) \tag{21}$$

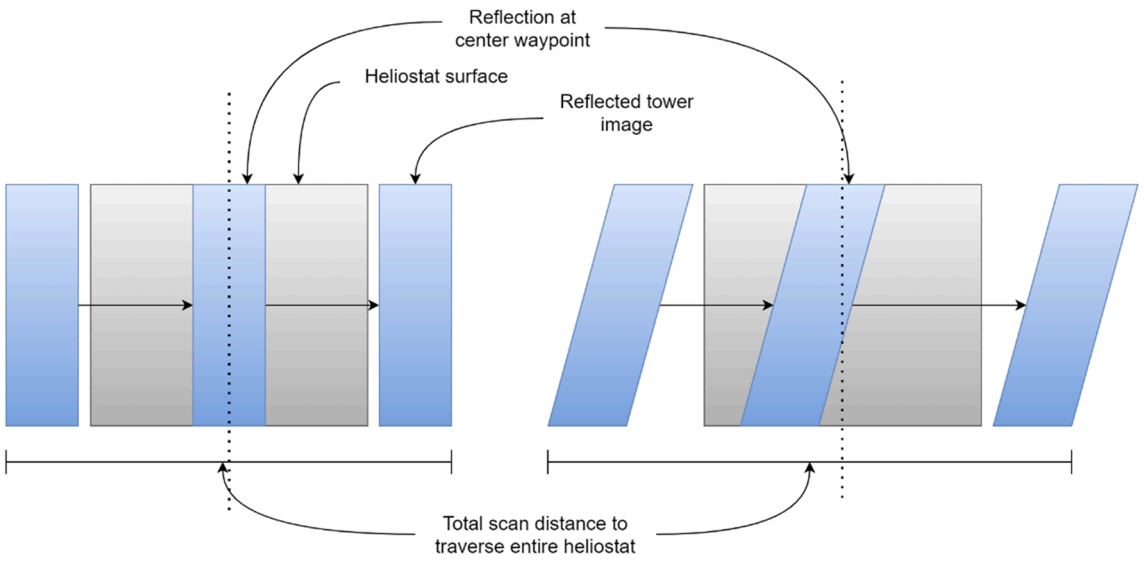

Fig. 20. Effect of reflection orientation on scan distance.

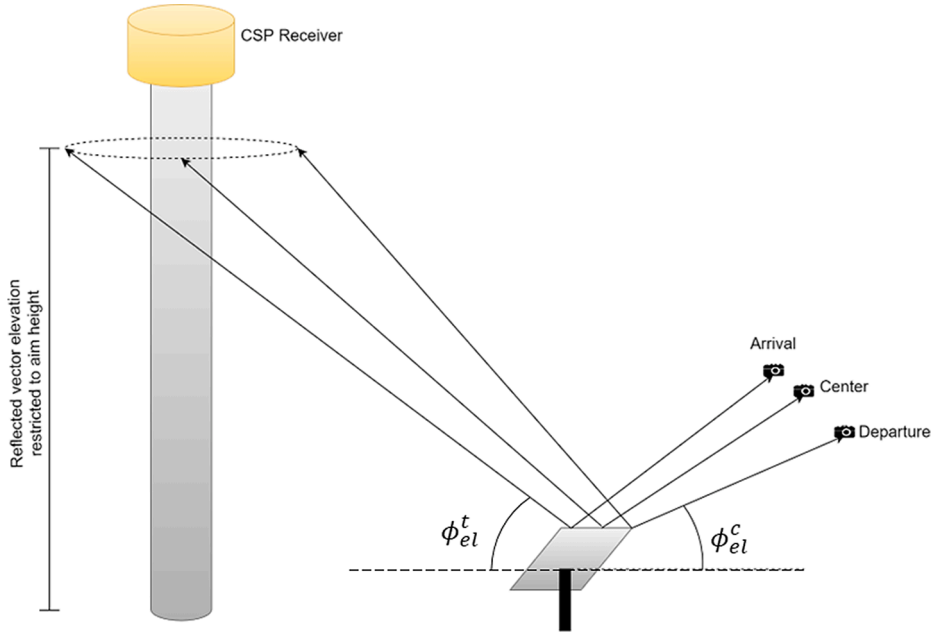

Fig. 21. Constraining the visible tower below the tower receiver.

If we conservatively assume the FOV is constant and equivalent to the FOV centered on the heliostat,[1] the angle must cover a distance d_{scan}^{min} at distance $d_t + d_c$ given a vertical tower reflection.

$$d_{scan}^{min} = d_{fov}^{t} + \varnothing_{tower} \tag{22}$$

The angle of the reflection, θ_r, increases the distance the reflection must traverse, as seen in Fig. 20. It expands d_{scan}^{min} by:

$$d_{scan} = d_{scan}^{min} + 2 \cdot \frac{h_l}{\tan(\theta_r)} \tag{23}$$

The scan angle, assuming a constant camera distance from the target, can be found by

$$\delta\theta_{fov} = 2 \cdot \tan^{-1}\left(\frac{d_{scan}}{2(d_c + d_t)}\right) \tag{24}$$

If the scan angle is thought of as a change in relative azimuth, or the azimuth of the UAS relative to the heliostat as in Fig. 19, the second component outputs an elevation by constraining the elevation of the reflected vector off the heliostat corners. The elevation at arrival and departure is constrained such that the glowing tower receiver is excluded from the image for an entire scan, see Fig. 21.

The elevation constraint places the camera at the peripherals at a set camera distance d_c, a set scan angle $+/- \frac{\delta\theta_{fov}}{2}$, and the elevation given by reflecting the vector from the aimpoint height off the top edge of the heliostat:

$$\phi_{el}^{c} = 2\phi_{el} - \phi_{el}^{t} \tag{25}$$

[1] The FOV in practice will be smaller, as the angle of incidence increases on the heliostat surface. This conservative assumption aids in creating waypoints that allow the UAS to effectively scan and focus with a buffer upon arrival and departure such that the tower reflection traverses completely across the heliostat.

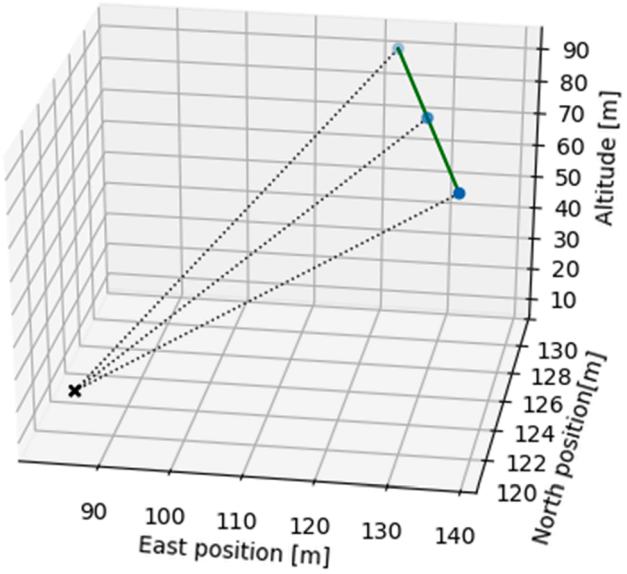

Fig. 22. Set of three waypoints for scanning a single heliostat, with dotted lines showing the camera pointing direction.

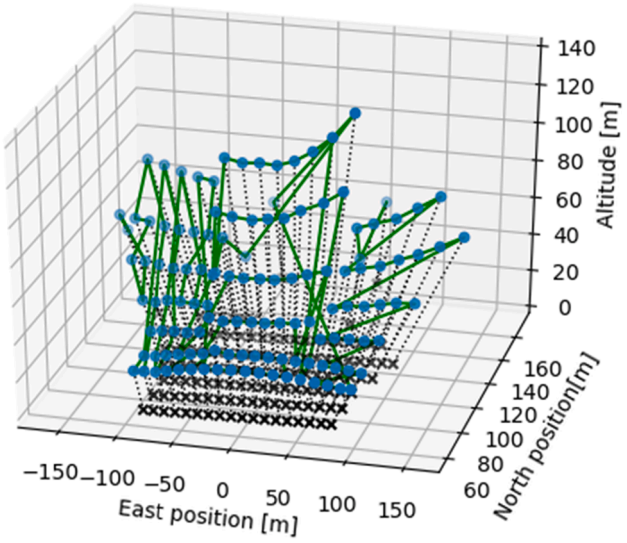

Fig. 23. Central waypoints over the NSTTF zone 1 heliostats. The heliostats are marked with an x.

Where ϕ_{el}^{t} is the elevation of the vector traced the top corner of the target heliostat to the tower aimpoint and ϕ_{el}^{c} is the resulting elevation of the vector traced from the top edge to the camera position d_c meters away. A set of 3 waypoints for measuring a single NSTTF heliostat is shown in Fig. 22.

The peripheral waypoints in local X, Y, Z coordinates can be computed from the camera distance d_c, the central waypoint, and the computed angles in Eq. (24).

3.7. Output parameters

The output of the above algorithm is a series of flight paths used to navigate a given field of heliostats. Each waypoint contains all the requisite data to:

- Position the UAS in space
- Point the camera toward the target heliostat
- Trigger the imaging hardware in the appropriate mode: video or still imaging
- Capture the reflected image of the receiver tower from the surface of the target heliostat.

The waypoints are appropriately scheduled to:

- Guide the UAS to target heliostats according to the path planner in Section 3.5
- Guide the UAS through a set of three scanning waypoints at each heliostat
- Guide the UAS to and from the base station location
- Pick up where the previous path terminated at the end of individual flights
- Pick up where the previous path terminated at the end of flight days using an updated field.

The waypoints are saved in file formats directly usable by UAS flight computers. Common interfaces include .csv and .xml file formats. The waypoint files may also be segmented and loaded sequentially, as flight computers that can save an NIO field path dictionary in its entirety are not common. A single field will contain tens of thousands of waypoints. An example flight path over the NSTTF zone 1 heliostats is seen in Fig. 23. The flight path shown only contains the central waypoint for clarity. At each of these noted UAS locations, there is a correpsonding arrival and departure waypoint as seen in Fig. 22.

4. Case study: Non-intrusive survey of the Crescent Dunes CSP plant under normal operation

The following case study shows implementation of the NIO path-planning method for a utility-scale CSP installation. The Crescent Dunes CSP installation is a commercial-sized solar plant in Tonopah, Nevada. The plant employs a field of over 10,000 heliostats concentrating thermal energy onto a receiver tower approximately 190 m in height. It allows for a full-scale implementation of the above method, which introduces several challenges not seen in a smaller, controlled environment. This case study scenario is the fully non-intrusive scenario, where the assumed plant condition is one of full operation with each heliostat actively tracking the sun. The output path allows for 1-dimensional measurements and will need to be performed twice to fully characterize 2D slope errors.

4.1. Facility overview

The installation comprises 10,348 heliostats over 1,650 acres. The

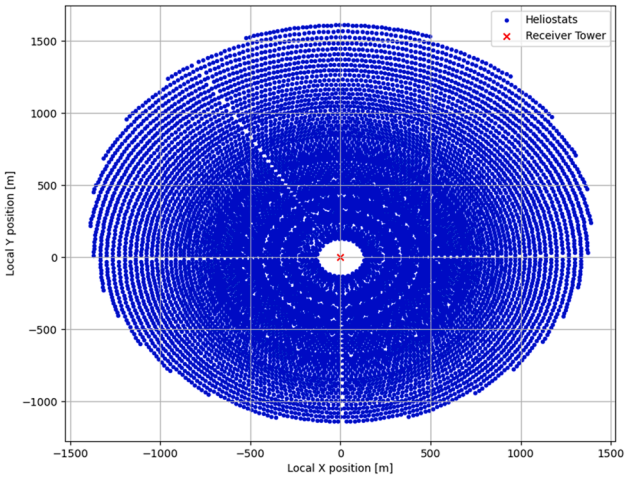

Fig. 24. Crescent Dunes heliostat field, comprising 10,348 heliostats.

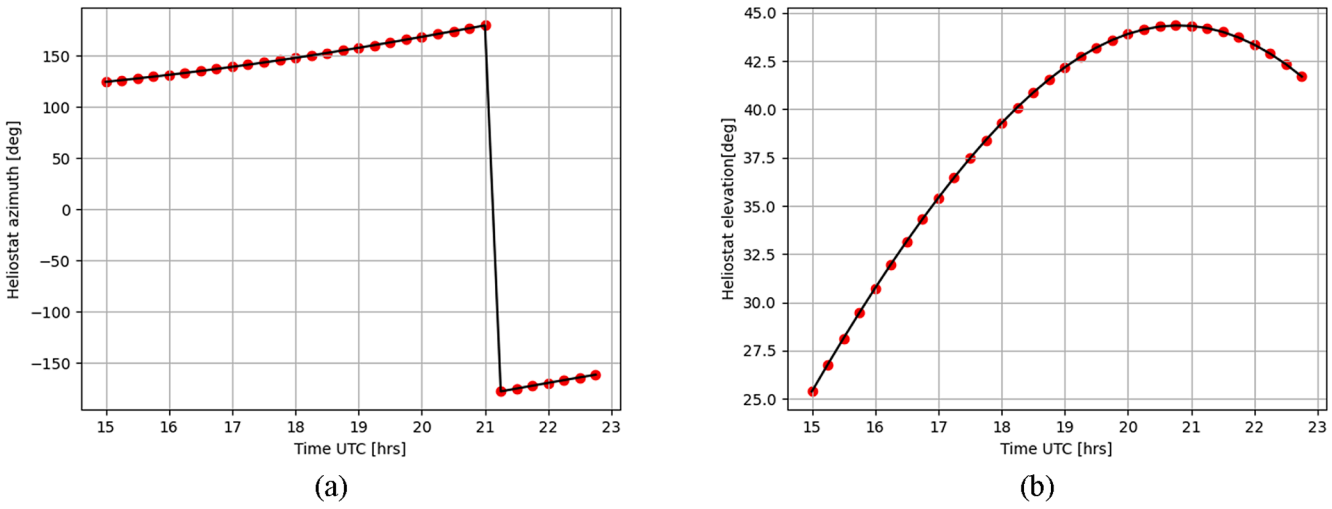

Fig. 25. Azimuth (a) and elevation (b) for a sample heliostat on June 21, 2020, from 15:00–23:00 UTC (PDT + 7). Orientations are recomputed every 15 min.

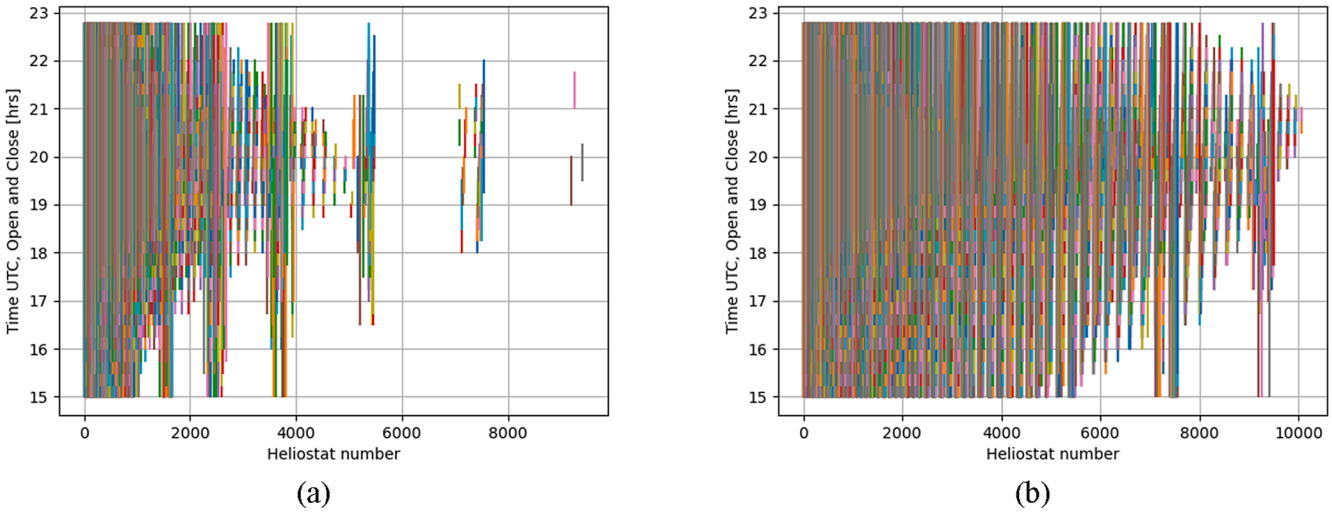

Fig. 26. Measurement windows for each of Crescent Dune's 10,348 heliostats. Vertical lines show each heliostat's open and close time in hours UTC with the field operational (a) and with obstructions stowed (b).

plant's tower stands approximately 190 m high and is cylindrical in shape. The field presents a commercially sized, realistic test environment for the NIO process.

4.2. Step-by-step output for commercial field

4.2.1. Case study input parameters

- Measurement start date: June 21, 2020
- Measurement start time: 15:00 UTC
- Field resolution: 15 min–4 orientations per hour
- Location: Tonopah, Nevada, Crescent Dunes CSP Plant
- UAS: Black Swift Technologies E2 Quadrotor
- Camera: Sony a5100 24.4 MP camera, APS-C sensor, 1.5x crop factor
- Lenses: 30, 45, 75, 127.5 mm (35 mm equivalent)

4.2.2. Step 1: Build a field

The Crescent Dunes model field is built using data provided by the power plant and shown in Fig. 24. The field includes all positioning and physical dimension data of the field's heliostats and receiver tower. Fig. 24 is shown in two dimensions for clarity; however, heliostat elevations are used in the algorithm's computations. Elevations in local coordinates are measured from zero at the tower base.

4.2.3. Step 2: Calculate orientations

Field orientations are calculated for each heliostat over the course of the input date at the chosen input resolution. The orientation for a given heliostat, as well as the incident sun vector, are shown in Fig. 25.

4.2.4. Step 3: Calculate measurement windows

Measurement windows are calculated by analyzing the heliostat orientations at the camera's maximum distance constrained by the camera's longest lens. In this study, a 127.5-mm lens is affixed to the Sony a5100, allowing a maximum effective imaging range of 121 m. At this range, a heliostat surface occupies 50% of the camera's FOV, allotting a pixel resolution of 1.75 pixels/cm. This pixel resolution is well within the tolerance for NIO image processing. Fig. 26 shows the compute measurement windows for the Crescent Dunes CSP plant, where the vertical lines span from the indexed heliostat's open time to close time.

4.2.5. Step 4: Subdivide field into focal zones

Using the measurement windows and available lenses, the field is subdivided into manageable sections based on lens focal lengths. Each

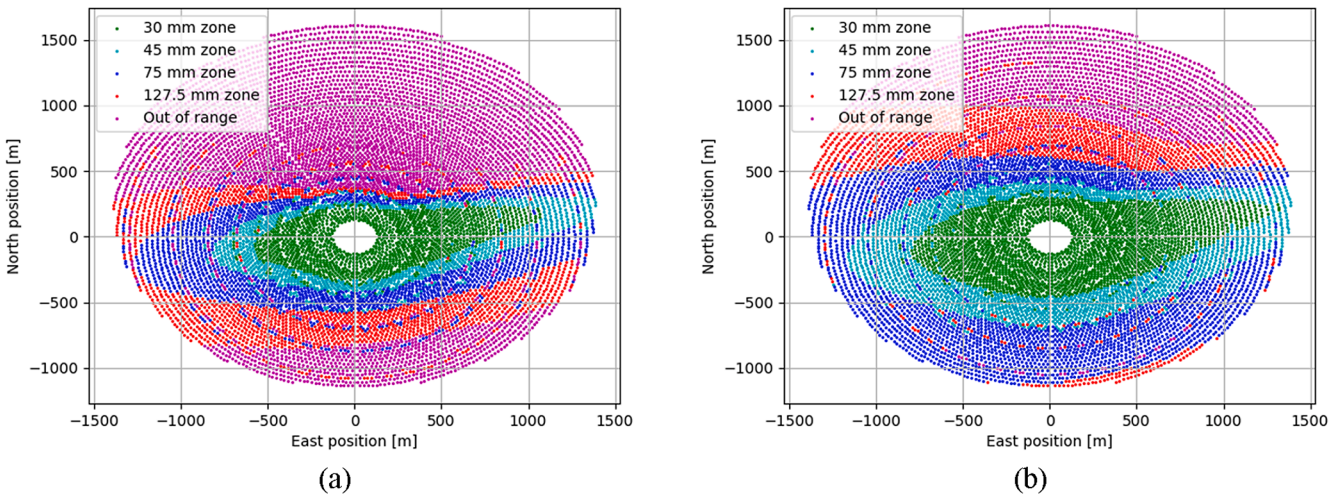

Fig. 27. Heliostats placed in zones based on focal length to be used for measurement with field operational (a) and with obstructions stowed (b).

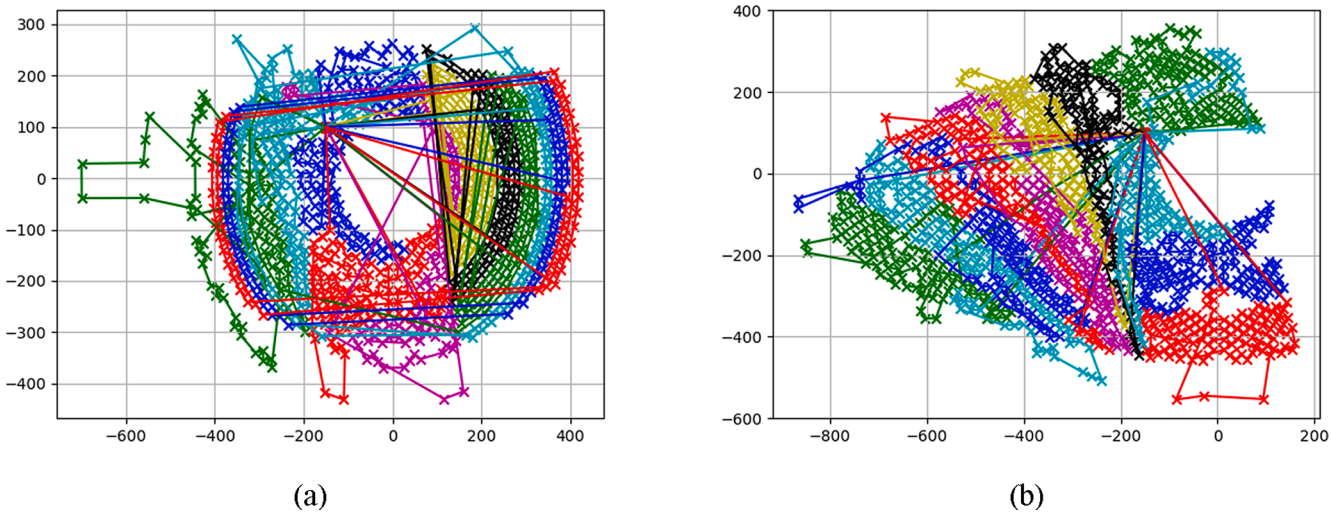

Fig. 28. Crescent Dunes flight paths over the Zone 1 heliostats for a single 8-hour day for field operational (a) and obstructions stowed (b).

lens change requires an imaging calibration, so the field is measured such that all heliostats using a particular lens are measured in a sequential set of flight paths prior to changing the lens.

Fig. 27 below shows the Crescent Dunes field divided into the zones set for the input date, imaging hardware, and available prime lenses. Note the ranges are for specific lenses and for achieving complete images. Image information is still attainable through accepting partial reflection data, where certain facets may be obstructed, or manipulating the heliostat into a measurable orientation.

The value of a partial heliostat scan should not be understated. In the cases where reflection data is available for a portion of a heliostat's facets, we can garner information about that heliostat's optical health based on the available facets' slope and canting, as well as infer characteristics about the heliostat's tracking error.

4.2.6. *Step 5: Plan paths and build flight schedule*

Once subdivided, the path planner is given a flight zone. The flight zone is visited sequentially according to the path planning approach in Section 3.5. The UAS visits target heliostats while tracking remaining flight time and time of day. Once flight time is exhausted, the UAS returns to the base station. Once the time of day is exhausted, the algorithm loads a subsequent field, and the process repeats. Shown in Fig. 28 are the flight paths for zone 1 in the Crescent Dunes field for a single 8-hour testing day. Following, in Fig. 29, is a sample path for an individual flight.

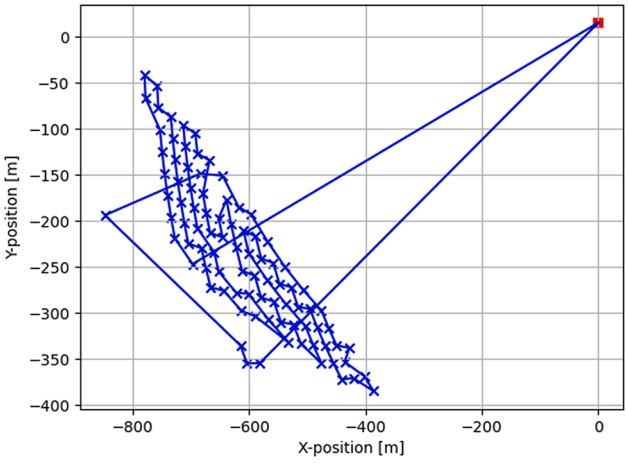

Fig. 29. Single flight for Crescent Dunes day 1 in zone 1 excerpted from the stowed field flights in Fig. 28 (b).

The algorithm is provided a scan time for each heliostat to ensure a

Table 4
Summary of flights for survey of entire Crescent Dunes installation.

Zone	Number of Heliostats	Flights	Average Heliostats per Flight
1: 30 mm	1609	11	146
2: 45 mm	1078	11	98
3: 75 mm	1877	23	81
4: 127.5 mm	1859	25	74
5: Partially blocked	3925	55	71
Totals	10,348	125	

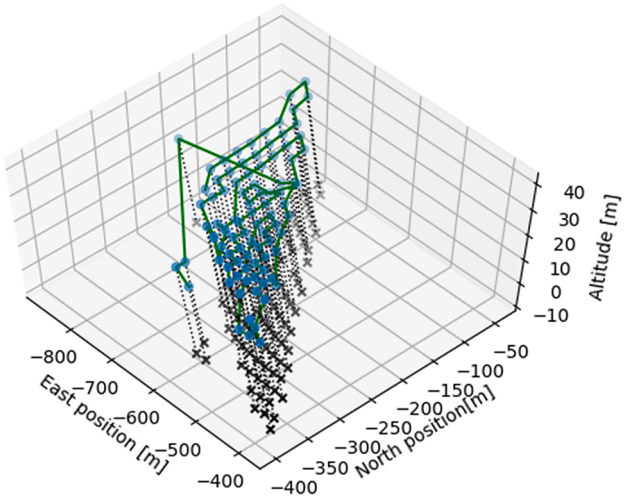

Fig. 30. Central waypoints for day 1 zone 1 flights shown in Fig. 29.

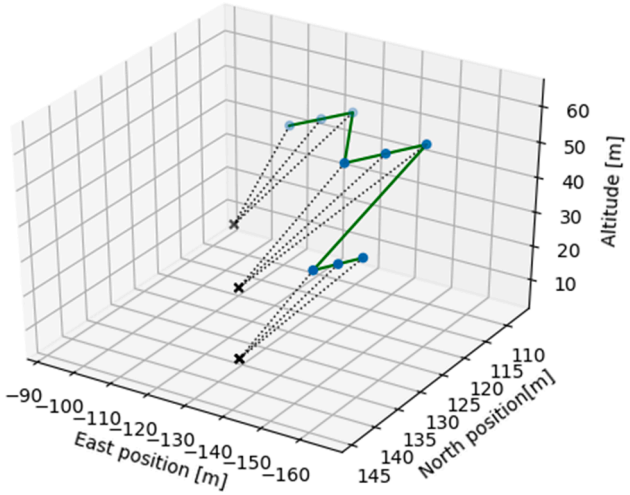

Fig. 31. Sets of three waypoints per heliostat excerpted from flight path in Fig. 30.

sufficient number of image frames. This implementation assumes 30 frames per second and a 10 s pass, resulting in 300 frames per heliostat. For a 20-meter pass, this yields an easily attainable velocity of 2 m/s. The algorithm assumes the aircraft can average 5 m/s during transits between heliostats and 10 m/s to and from the base station. When the algorithm is run for an entire field, the result is a total of 125 flights over 12 days. For completeness, Zone 5 contains heliostats that are partially blocked, but are still included in the flight planner. A summary is available in Table 4.

Table 5
Areas to reduce time required for measuring a full, operational plant.

Algorithm Update	Impact
Introduce dynamic constraints	Reduces acute turns and accelerations that may impact the aircraft's velocity and battery efficiency
Update velocity parameters with experimental data	Modern UAS available to plant operators may be considerably more agile than the UAS used in this case study
Post-waypoint optimization	Heliostats as the point of optimization is useful in initial computation, but each heliostat has 3 waypoints. Adding an additional tier of path optimization may fine-tune the path and save additional flight time
Waypoint simplification and reduction	Each heliostat has 3 waypoints for maximum measurement granularity. Trading some granularity for a flight path simplification that results in longer, straighter paths may save additional flight time. This is a strong candidate in the near field, where elevation angles are typically higher and blocking is less of a concern.
Multiple UAS	A CSP installation offers ample airspace to operate several UAS safely and simultaneously. The personnel required to operate each aircraft is minimal. Flight times can be greatly reduced by flying multiple aircraft.

4.2.7. Step 6: Generate waypoints

Each sequential path of heliostats is converted to a series of flight-computer compatible waypoints. A sample path tracing the central waypoints is seen in Fig. 30. A detailed view of a subset of heliostats and the corresponding measurement scans is seen in Fig. 31. Full sets of waypoints are computed for each path output in Section 4.2.6.

5. Discussion

With plants currently suffering from significant power output and cost losses due to optical degradation, this UAS path planning algorithm provides one efficient, feasible way to measure optical degradation that impacts plant efficiency. Below, the major positive benefits of the method are explained:

5.1. Large-scale optical data

Though optical data has successfully been collected on a small scale, it has never been done on a large scale. This method could facilitate the creation of a substantial data set, consisting of optical errors collected for thousands of heliostats. It would allow for the first complete and comprehensive assessment of the optical performance of a plant and would be immensely useful for future research and development efforts to design more efficient heliostats and plant layouts and to optimize plant maintenance operations.

5.2. Efficient data collection

The UAS-based data collection allows for rapid optical surveying; only a few seconds are required to survey a single heliostat with the NIO method. The optimized drone path planning allows for a full-field survey that when optimally scheduled under this set of parameters, can be accomplished within 12 days. A full characterization of 2D slope errors then takes 24 days. The commanded speeds for the case study in 4.2.6 are conservative, with modern UAS capable of speeds up to 30 m/s and video frame rates reaching 120 frames per second. Modeling faster, more agile aircraft with these modern parameters would yield an even faster estimate for survey completion.

5.3. Improvement

In addition to tuning the velocity parameters on the UAS, additional

Table 6
Measurement availability and utility under various operational conditions for an entire CSP plant.

meas. Criteria	UTILITY	Field condition	Measurement criteria	% Field meas. for April 15th, 2021
5. Most restrained	Focused field monitoring	Fully operational	Full, unobstructed measurements	48.3%
4.	Broad field monitoring	Fully operational	Partial measurements acceptable*	59.2%-98.3%
3.	Focused performance enhancement	May manipulate obstructing heliostats	Full, unobstructed measurements	62.4%
2.	Broad performance enhancement	May manipulate obstructing heliostats	Partial measurements acceptable*	92.6–100%
1. Least restrained	Full-field error calibration & controlled environment characterization	May manipulate obstructing and target heliostats	Full, unobstructed measurements	100%

optimization parameters may be introduced to limit turning angles and velocity changes, yielding flight plans more considerate of UAS flight dynamics. The current optimization prioritizes measurability. Further reductions in time commitment can be made by prioritizing flight times and restricting longer transits that often result when the algorithm ignores closer heliostats when seeking out heliostats deemed more measurable. Each of these are expected to reduce the projected time required to scan the entire installation and are topics of future research. The case study above shows that we are capable of performing this survey at the present. Future improvements may show significant reductions to the required time commitment. Table 5 below shows strong candidates to further reduce the time commitment required to measure a full installation.

5.4. Automation

The UAS data collection is nearly entirely autonomous, requiring only a handful of workers to operate the drone. Significant personal time and costs are saved through the use of this method.

5.5. Addressing potential obstacles

Below, some potential obstacles that could limit the success of the UAS optical survey are addressed:

5.5.1. Schedule deviations

Deviations between the planned flight time and actual flight time could impact the collected image data. Operation constraints in the field could cause the testing schedule to drift from the planned procedure, in which case the heliostat orientations will differ from those for which the waypoints were precalculated. To mitigate this issue, paths can be recalculated dynamically in the field based on the real-time schedule. The runtime of the algorithm falls within the battery cycle life of the drone, so paths could easily be recalculated between each battery change. In addition, UAS are in constant contact with the ground station. High-end UAS allow path deviations and updates to be sent in real time, allowing for corrections to be uploaded mid-flight.

5.5.2. Solar flux

In some parts of the field, the drone must fly very high to capture viable images (100–150 m). This could put the drone in danger of flying close to the sunbeams of the heliostat. Care will need to be taken to ensure the path does not take the drone in a region that would exceed its safe operating temperature. Additionally, flying close to the sun vector can cause glare in the images, which can negatively impact the image processing. The flight height of the drone can be reduced by stowing some groups of blocking heliostats so that a viable image can be taken at a lower altitude.

5.5.3. Environmental and seasonal conditions

Environmental conditions such as high winds can impact the operation of the drone. If wind causes the drone position to shift from its calculated position, it will offset the point of interest of the camera. This only becomes a problem if the target heliostat leaves the frame of the FOV. This issue can be mitigated by decreasing the focal length, so the heliostat occupies a smaller portion of the FOV, allowing for more margin of error if the camera position is varying.

The time of year can impact the data collection process. In the above examples, the sun's trajectory is as long as it will be throughout the year. As the sun trajectory shortens and the range of elevations decreases, some heliostats' measurability may be adversely affected. In winter seasons, blocking may become more apparent.

5.5.4. Partial measurements and heliostat manipulation

The goal of the NIO method is to present a non-intrusive method for plants to characterize optical errors in heliostats. The case studies above show that these measurements may be prohibitively difficult to obtain under normal operation. In many cases, there will be some obstruction to the heliostats measured in-situ. Though the ideal case is a completely clear reflection spanning each row of facets, a partial measurement's value should not be understated. Even a partial measurement offers valuable insight into the optical health of a heliostat.

In cases where a full characterization is needed and the heliostat is blocked, heliostats may be manipulated to achieve the required image data. In this case, a heliostat may be manually oriented and fixed in a design orientation that allows for a clear measurement. If a full characterization is necessary, the heliostat is already likely underperforming. In this case, taking the heliostat offline briefly to characterize the optical errors is of low impact to the plant.

5.6. NIO survey under various conditions

The NIO method is concerned with the optical error characterization of each heliostat in a given plant. The fully non-intrusive method is the primary approach, but several measurement scenarios exist that may increase measurability if the non-intrusive scan dictates a more granular set of data. The potential scenarios along with the effects on heliostat measurability are laid out below in Table 6. Each scenario presents a utility and a field condition as well as the impact on measurability. The right most column in the table shows the percentage of the field available to measure while meeting the listed Field Condition. We envision a fully non-intrusive survey will yield sufficient optical health information to warrant additional measurements taken under the conditions presented below.

6. Conclusions

Each section of this paper demonstrates a piece of the sequential path-planning algorithm. The result lends credence to the applicability of a UAS to collect large volumes of precise imaging data. Currently, no technology or approach exists to accurately measure the three stated sources of heliostat error. NIO not only provides a means to analyze

these errors using image data, but a way to collect the immense amount of data necessary. The results show a step-by-step process for setting up a flight plan for any commercially available UAS capable of autonomous flight. The output is a series of flight paths in a geolocated coordinate system usable by flight computers in a desired format. The output waypoint files include all requisite data to position the UAS, point the imaging hardware, collect the images, and sequence through a series of targets, while the constraints imposed ensure those images are within the required tolerances to be used to characterize optical errors.

The implementation of the flight planning process demonstrates the application of UAS to CSP error characterization as a viable and useful tool for collecting NIO method image data. Using a UAS to collect the data is more efficient, less costly, and allows for repeatable, rigorous data collection plans that operate autonomously, requiring minimal personnel. The UAS allows camera positioning and image collection that would otherwise require significant manipulation of the installation's heliostats, significant time commitment from operators, and inconsistent imaging data across repeated test campaigns if the data is collected manually.

In future work, improvements will be made to the path planning algorithm to increase its efficiency and reliability. Simulations can be used to test the sensitivity of the path planner to the previously mentioned conditions such as changing environmental conditions, solar flux, and schedule deviations. Safe operating parameters will be defined to allow for safe and successful completion of the drone survey. The drone optical survey will be tested at a commercial plant to validate its effectiveness and to determine unforeseen operation obstacles. Analyses involving the sensitivity of the UAS to environmental factors will be included in the path planner.

Declaration of Competing Interest

The authors declare that they have no known competing financial interests or personal relationships that could have appeared to influence the work reported in this paper.

Acknowledgments

This work was authored by employees from the National Renewable Energy Laboratory, operated by Alliance for Sustainable Energy, LLC, for the U.S. Department of Energy (DOE) under Contract No. DE-AC36-08GO28308. Funding provided by U.S. Department of Energy Office of Energy Efficiency and Renewable Energy (EERE) Solar Energy Technologies Office (SETO). The views expressed in the article do not necessarily represent the views of the DOE or the U.S. Government. The U.S. Government retains and the publisher, by accepting the article for publication, acknowledges that the U.S. Government retains a nonexclusive, paid-up, irrevocable, worldwide license to publish or reproduce the published form of this work, or allow others to do so, for U.S. Government purposes.

The authors would also like to acknowledge our colleagues from Sandia National Laboratories, Dr. Dan Small, Dr. Julius Yellowhair, Dr. David Novick, and supporting staff at NSTTF for the raw data collection and very helpful discussions during the development of the NIO method.

References

Kincaid, N., et al., 2018. An optical performance comparison of three concentrating solar power collector designs in linear Fresnel, parabolic trough, and central receiver. Applied Energy 231, 1109–1121.
Wagner, M.J., Wendelin, T., 2018. SolarPILOT: A power tower solar field layout and characterization tool. Solar Energy 171, 185–196.
Olewitz, C., 2016. Take a peek inside Nevada's new solar farm that generates power 24/7 with molten salt. 2016; Available from: https://www.digitaltrends.com/cool-tech/peek-inside-nevada-solar-plant-247-power-molten-salt/.
Stynes, J., Ihas, B., 2012. Slope Error Measurement Tool for Solar Parabolic Trough Collectors. Preprint.
Stynes, J., Ihas, B., 2012. Absorber Alignment Measurement Tool for Solar Parabolic Trough Collectors: Preprint.
Ren, L., et al., 2014. A review of available methods for the alignment of mirror facets of solar concentrator in solar thermal power system. Renewable and Sustainable Energy Reviews 32, 76–83.
King, D.L., 1982. Beam quality and tracking-accuracy evaluation of second-generation and Barstow production heliostats.
Strachan, J., 1992. Revisiting the BCS, a measurement system for characterizing the optics of solar collectors.
Belhomme, B., et al., 2009. A New Fast Ray Tracing Tool for High-Precision Simulation of Heliostat Fields. Journal of Solar Energy Engineering 131.
Arqueros, F., Jiménez, A., Valverde, A., 2003. A novel procedure for the optical characterization of solar concentrators. Solar Energy 75 (2), 135–142.
Röger, M., Prahl, C., Ulmer, S., 2008. Fast Determination of Heliostat Shape and Orientation by Edge Detection and Photogrammetry.
Paré, E., et al., 2002. CELESTE: an atmospheric Cherenkov telescope for high energy gamma astrophysics. Nuclear Instruments and Methods in Physics Research Section A: Accelerators, Spectrometers, Detectors and Associated Equipment 490 (1), 71–89.
Prahl, C., et al., 2011. Airborne Shape Measurement of Parabolic Trough Collector Fields.
Strachan, J., Houser, R., 1993. Testing and evaluation of large-area heliostats for solar thermal applications.
Ulmer, S., et al., 2011. Automated high resolution measurement of heliostat slope errors. Vol. 85.
Goldberg, N., et al., 2015. Embedding a Visual Range Camera in a Solar Receiver. Energy Procedia 69, 1877–1884.
Goldberg, N., Zisken, A., 2015. Heliostat Surface Estimation by Image Processing. Energy Procedia 69, 1885–1894.
Mitchell, R.A., Zhu, G., 2020. A non-intrusive optical (NIO) approach to characterize heliostats in utility-scale power tower plants: Methodology and in-situ validation. Solar Energy 209, 431–445.
Mitchell, R., Zhu, G., 2020. A Non-Intrusive Optical (NIO) Approach to Characterize Heliostats in Utility-Scale Power Tower Plants. Sensitivity Study.
Obermeyer, K., 2009. Path Planning for a UAV Performing Reconnaissance of Static Ground Targets in Terrain.
Ferris, D., et al., 2018. Time-Optimal Multi-Waypoint Mission Planning in Dynamic. Environments. 1–8.
Likhachev, M., et al., 2005. Anytime Dynamic A*: An Anytime. Replanning Algorithm. 262–271.
Ishida, S., Rigter, M., Hawes, N., 2019. Robot Path Planning for Multiple Target Regions, 1-6.
Davidov, D., Markovitch, S., 2006. Multiple-Goal Heuristic Search. J. Artif. Intell. Res. (JAIR) 26, 417–451.
Peter Hart, N.J.N., Raphael, B., 1968. A Formal Basis for the Heuristic Determination of Minimum Cost Paths. IEEE Transactions of Systems Science and Cybernetics.